LJMU Research Online

Cosentino, G, Jiménez-Serra, I, Barnes, AT, Tan, JC, Fontani, F, Caselli, P, Henshaw, JD, Law, C-Y, Viti, S, Fedriani, R, Hsu, C-J, Gorai, P, Zeng, S and De Simone, M

 Interaction between the supernova remnant W44 and the infrared dark cloud G034.77-00.55: Shock induced star formation

http://researchonline.ljmu.ac.uk/id/eprint/25317/

Article

Astronomy & Astrophysics

Interaction between the supernova remnant W44 and the infrared dark cloud G034.77-00.55: Shock induced star formation

G. Cosentino[1,★] , I. Jiménez-Serra[2] , A. T. Barnes[1], J. C. Tan[3,4], F. Fontani[5] , P. Caselli[6], J. D. Henshaw[7],
C.-Y. Law[5], S. Viti[8], R. Fedriani[9] , C.-J. Hsu[3], P. Gorai[10,11] , S. Zeng[12] , and M. De Simone[1,5]

[1] European Southern Observatory, Karl-Schwarzschild-Strasse 2, 85748 Garching, Germany
[2] Centro de Astrobiología (CSIC/INTA), Ctra. de Torrejón a Ajalvir km 4, Madrid, Spain
[3] Department of Space, Earth and Environment, Chalmers University of Technology, 412 96 Gothenburg, Sweden
[4] Department of Astronomy, University of Virginia, 530 McCormick Road Charlottesville, 22904-4325 USA
[5] INAF Osservatorio Astronomico di Arcetri, Largo E. Fermi 5, 50125 Florence, Italy
[6] Max Planck Institute for Extraterrestrial Physics, Giessenbachstrasse 1, 85748 Garching bei München, Germany
[7] Astrophysics Research Institute, Liverpool John Moores University, 146 Brownlow Hill, Liverpool L3 5RF, UK
[8] Leiden Observatory, Leiden University, PO Box 9513, 2300 RA Leiden, The Netherlands
[9] Instituto de Astrofísica de Andalucía, CSIC, Glorieta de la Astronomía s/n, 18008 Granada, Spain
[10] Rosseland Centre for Solar Physics, University of Oslo, PO Box 1029 Blindern, 0315 Oslo, Norway
[11] Institute of Theoretical Astrophysics, University of Oslo, PO Box 1029 Blindern, 0315 Oslo, Norway
[12] Star and Planet Formation Laboratory, Cluster for Pioneering Research, RIKEN, 2-1 Hirosawa, Wako, Saitama 351-0198, Japan

ABSTRACT

Context. We have studied the dense gas morphology and kinematics towards the infrared dark cloud (IRDC) G034.77-00.55, shock-interacting with the SNR W44, to identify evidence of early-stage star formation induced by the shock.
Aims. We used high angular resolution $N_2H^+(1–0)$ images across G034.77-00.55, obtained with the Atacama Large Millimeter/sub-Millimeter Array. N_2H^+ is a well-known tracer of dense and cold material, optimal for identifying gas that has the highest potential to harbour star formation.
Methods. The N_2H^+ emission is distributed in two elongated structures, one towards the dense ridge at the edge of the source and one towards the inner cloud. Both elongations are spatially associated with well-defined mass-surface density features. The velocities of the gas in the two structures (i.e. 38–41 km s^{-1} and 41–43 km s^{-1}) are consistent with the lowest velocities of the J- and C-type parts, respectively, of the SNR-driven shock. A third velocity component is present at 43–45.5 km s^{-1}. The dense gas shows a fragmented morphology with core-like fragments at scales consistent with the Jeans lengths, masses of $\sim$1–20 M$_\odot$, densities of ($n(H_2) \geq 10^5$ cm^{-3}) sufficient to host star formation in free-fall timescales (a few 10^4 yr), and with virial parameters that suggest a possible collapse.
Results. The W44 driven shock may have swept up the encountered material, which is now seen as a dense ridge, almost detached from the main cloud, and an elongation within the inner cloud, well constrained in both N_2H^+ emission and mass surface density. This shock compressed material may have then fragmented into cores that are either in a starless or pre-stellar stage. Additional observations are needed to confirm this scenario and the nature of the cores.

Key words. ISM: bubbles – ISM: clouds – ISM: molecules – ISM: supernova remnants – ISM: individual objects: W44 – ISM: individual objects: G034.77-00.55

1. Introduction

It is known that stars are born from the collapse of molecular clouds, which are the coldest (T<25 K; Pillai et al. 2006; Rathborne et al. 2006) and densest ($n(H_2)>10^2$ cm^{-3}, Chevance et al. 2023) regions of the interstellar medium (ISM). However, the processes that initiate cloud collapse in these objects are still unclear (e.g. Tan 2000; Tan et al. 2014; Hernandez & Tan 2015; Peretto et al. 2016; Retes-Romero et al. 2020; Morii et al. 2021). Supernova explosions (SNes) and remnants (SNRs) are among the most powerful events in galaxies (energy of detonation $\sim$10^{50}–10^{51} ergs; Koo et al. 2020) and are thought to play a pivotal role in setting the low levels of star formation efficiency observed in the local universe ($\epsilon \sim$ 1–2%; Krumholz et al. 2012). However, it is still debated whether SNR feedback

can efficiently trigger star formation in molecular clouds. For a detailed discussion of the complexity and challenges of this problem, both observationally and theoretically, we refer to Dale et al. (2015). In particular, it is difficult to assess the importance of SNR shocks (and other bubbles) in sweeping up material, and hence forming clouds (see e.g. Inutsuka et al. 2015) or how pre-existing clouds affect the shock propagation. Recent observational works seem to indicate that SNR feedback may be able to significantly increase the cloud gas density (Inoue et al. 2018; Cosentino et al. 2019, 2022; Sano et al. 2020, 2023) and the star formation efficiency of galaxies up to 40% (Rico-Villas et al. 2020), but more observational work is needed to inform existing models (Ceverino & Klypin 2009; Dale 2015).

Here we investigate the dense gas morphology and kinematics towards the infrared dark cloud (IRDC) G034.77-00.55 (hereafter G034.77; Fig. 1), known to be shock-interacting with

---

★ Corresponding author; giuliana.cosentino@eso.org
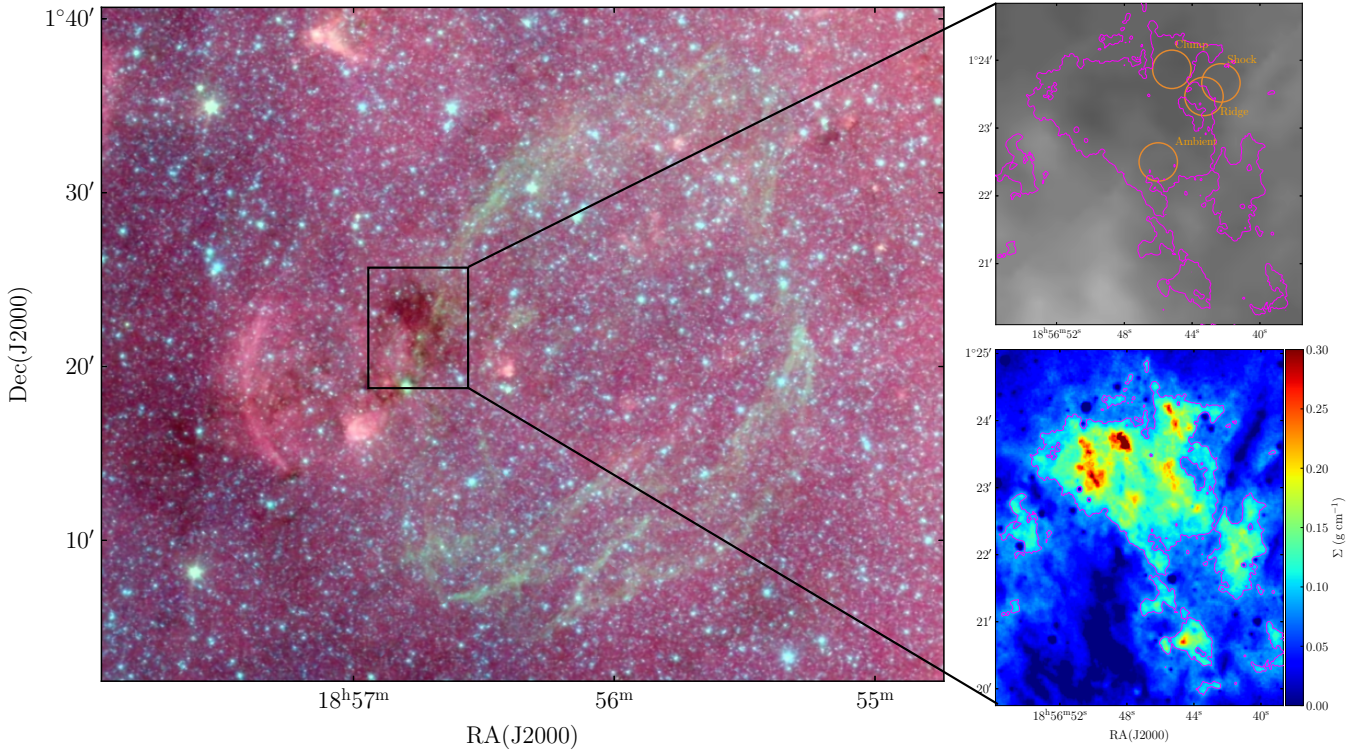
Fig. 1. Multi-spatial scale and multi-wavelength view of the SNR W44 and the nearby cloud G034.77. *Left*: three-color image of G034.77 together with the SNR W44 and the HII region G034.758-00.681. Red is 8 μm, green is 5.8 μm, and blue is 4.5 μm emission from the *Spitzer* GLIMPSE survey (Churchwell et al. 2009). *Right top*: *Hershel* 70 μm images of G034.77; the positions for which the D/H ratios were obtained in this work are overlaid as orange circles. The aperture size is 34″, i.e. the largest aperture in our data. *Right Bottom*: mass surface density map (colour scale) of G034.77 (Kainulainen & Tan 2013). In both panels, the Σ=0.09 g cm^{-2} contour, equivalent to a visual extinction A$_V$= 20 mag is shown in magenta.

the SNR W44 (Wootten 1978; Castelletti et al. 2007; Cardillo et al. 2014). W44 is a core-collapse SNR of ∼20k years and located at a distance of 2.9 kpc (Lee et al. 2020). Today classified as a mixed-morphology SNR (i.e. with a shell-like morphology in the radio wavelengths and centrally filled in the X-rays; Rho & Petre 1998), W44 was first identified as a radio source by Westerhout (1958), then classified as a SNR by Scheuer (1963), and later observed in X-ray by Gronenschild et al. (1978). Only more recently were gamma-ray observations with Fermi-LAT reported (Abdo et al. 2010). W44 shows a strong elliptical morphology that has long been interpreted as being due to the shell expanding into the inhomogeneous interstellar medium (ISM). Evidence of interaction between the SNR and the surrounding material has been reported at multiple wavelengths (e.g. Reach et al. 2005, 2006). Towards the source to the north-west, a bright radio emission is associated with atomic line emission characteristic of shock-excited radiative filaments (Giacani et al. 1997). Moreover, towards the same region, Yoshiike et al. (2013) used CO emission lines to identify highly excited molecular gas associated with the SNR shell. Towards several regions across the W44, OH maser emission at 1720 MHz has been reported, which is known to indicate sites of ongoing C-type shock interactions (Hoffman et al. 2005). Finally, towards the south-east, W44 is known to be expanding into the dense molecular cloud G034.77. The cloud was first identified by Wootten (1978) via CO observations, and later classified as an infrared dark cloud by Simon et al. (2006) using the Midcourse Space Experiment. The authors also reported that the cloud is located at a distance of 2.9 kpc (consistent with the value inferred for W44). Since then, the cloud has been largely studied as a stand-alone source, part of

the large sample of Rathborne et al. (2006), but also as part of the Butler & Tan (2009) sample (e.g. Hernandez & Tan 2015). The interaction between the cloud and the SNR has also been investigated. Castelletti et al. (2007) reported strong evidence of interaction using VLA radio emission, while Cardillo et al. (2014) reported evidence of cosmic ray acceleration. Sashida et al. (2013) used HCO$^+$ single-dish maps to infer a shell expansion velocity of ∼13 km s^{-1}. Thanks to its relative closeness, mid-age, and slow shock, as well as its clear association with a dense cloud, W44 is one of the best galactic candidates to study in detail the effect of the interactions between SNRs and molecular clouds. Recently, we have used ALMA images of the J=2−1 silicon monoxide (SiO) emission to study the shock interaction between the cloud and the SNR (Cosentino et al. 2018, 2019). SiO is a unique shock tracer because its abundance is usually very low in quiescent regions, but is extremely enhanced in the presence of shocks where dust sputtering occurs (Martin-Pintado et al. 1992; Jiménez-Serra et al. 2005). From the high angular resolution ALMA images, the SiO emission is organised into two elongated structures caught in the act of decelerating (from ∼46 km s^{-1} to ∼39 km s^{-1}) and plunging into a dense ridge at the edge of G034.77. The plunging shock enhances the ridge gas density by a factor >10 (i.e. to values n(H$_2$)>10^5 cm^{-3}) comparable to those required to enable star formation (Cosentino et al. 2019; Parmentier et al. 2011). From Cosentino et al. (2019), the SiO kinematic structure is best reproduced by a CJ-type time-dependent magnetohydrodynamic (MHD) shock propagating into the cloud at a velocity of ∼20 km s^{-1}, consistent with that measured by Sashida et al. (2013) using HCO$^+$(1–0) observations.

More recently, we used IRAM-30 m single pointing observations of $N_2H^+(1-0)$ and $N_2D^+(1-0)$ to investigate the deuterium fractionation across the shock front (Cosentino et al. 2023). The D/H ratio is a well-studied tracer of cores on the verge of gravitational collapse, when enhanced by several orders of magnitude (Crapsi et al. 2005; Caselli et al. 2008; Emprechtinger et al. 2009) with respect to the cosmic D/H abundance ($\sim 10^{-5}$; Oliveira et al. 2003). In these regions the molecular material is very dense $(n(H_2) > 10^4$ cm^{-3}) and cold (T<20 K, Awad et al. 2014; Fontani et al. 2015) and CO is highly depleted from the gas phase. All this boosts the root reaction of many deuterated molecules (Gerlich et al. 2002). Towards the dense ridge, the reported D/H ratios lie in the range $\sim 0.05-0.1$, consistent with what is typically measured in starless and pre-stellar cores (Fontani et al. 2011; Emprechtinger et al. 2009; Kong et al. 2016; Cheng et al. 2021). These values are also a factor of >2–3 larger than the D/H ratio measured towards an inner region of the cloud and known as Ambient (Cosentino et al. 2023). Finally, the deuterated gas velocity is consistent with that of the post-shocked gas probed by $C^{18}O$ (Cosentino et al. 2019), suggesting that the starless and pre-stellar cores may have formed by the interaction of the shock.

For this work, we complemented the IRAM-30 m spectra presented in Cosentino et al. (2023) with APEX observations of the J=3→2 N_2H^+ and N_2D^+ transitions, and used a multi-line approach to estimate the D/H ratio across the shock front. Hence, we used the $N_2H^+(1-0)$ ALMA images from Barnes et al. (2021) to investigate the morphology and kinematics of the dense gas across and near the shock. N_2H^+ is a well-known tracer of dense and cold material, where its destroyer CO depletes much faster than its precursor N_2 (Caselli et al. 2002). Therefore, N_2H^+ has also been widely used to identify cold cores in molecular clouds (e.g. Pirogov et al. 2003; Tatematsu et al. 2004; Fontani et al. 2006; Liu et al. 2019). The paper is organised as follows. In Sect. 2, we describe the new observations and archival data used in this work. In Sect. 3 we obtain new, more accurate, estimates of the D/H ratios across the shock front. In Sects. 4 and 5, we investigate the $N_2H^+(1-0)$ morphology and kinematics, using the archival ALMA images. Finally, in Sect. 6, we discuss our results and present our conclusions.

2. Observations and data

2.1. APEX and IRAM-30 m observations

In March 2020 we obtained high-sensitivity single pointing observations of the N_2H^+ and N_2D^+ J=1–0 transitions towards five positions across the IRDC G034.77 (Cosentino et al. 2023). For a complete description of the IRAM-30 m observations we refer to Cosentino et al. (2023). The five positions were chosen to be representative of different physical conditions across the cloud. In particular, the positions labelled 'Clump', 'Ridge', and 'Shock' are located towards the shock front probed by the SiO emission (Cosentino et al. 2019) and are representative of a dense clump adjacent to the shock front, the dense ridge, and the SiO emission peak (see Fig. 1 in Cosentino et al. 2018). Towards these three positions, in July 2023 we used Atacama Path-Finder Experiment (APEX) to obtain high-sensitivity single-pointing observations of the N_2H^+ and N_2D^+ J=3–2 transitions. In Fig. 1 (top left panel) the three positions of interest are shown (orange circles), together with the location of the Ambient region. In Cosentino et al. (2023) the Ambient position was selected as being representative of the bulk of the cloud (i.e. the inner gas within G034.77 with velocity $\sim$43 km s^{-1}).

Table 1. Equatorial coordinates of the positions analysed in this work.

Position	RA(J2000) (hh:mm:ss)	Dec(J2000) (dd:mm:ss)
Shock	18:56:42.3	01:23:40
Ridge	18:56:43.4	01:23:28
Clump	18:56:45.2	01:23:52

For the three positions of Clump, Ridge, and Shock, observations were performed in position switching mode (off-position RA(J2000)=$18^h57^m01^s$, Dec(J2000)=$1^d22^m25^s$) and dual polarisation mode. The nFLASH240 receiver was used with tuning frequencies 231.320 and 279.512 GHz and frequency resolution 488 kHz. At the selected tuning frequencies, the velocity resolutions and beam sizes are 0.7 km s^{-1} and 27″ for $N_2D^+(3-2)$, 0.5 km s^{-1} and 23″ for $N_2H^+(3-2)$. For comparison, the IRAM-30 m spectra presented in Cosentino et al. (2023) have a spectral resolution of $\sim$0.7 km s^{-1} and beam sizes 34″ and 27″ for $N_2D^+(1-0)$ and $N_2H^+(1-0)$, respectively. Observations were obtained in units of antenna temperature T_A^*, and converted to main beam temperature T_{mb} using a beam and forward efficiency of 0.77 and 0.95, respectively. The achieved rms are 3 mK for $N_2D^+(3-2)$ and 7 mK for $N_2H^+(3-2)$, while Cosentino et al. (2023) report rms of 5 mK for $N_2D^+(1-0)$ and 7 mK for $N_2H^+(1-0)$. In Table 1, the coordinates of the positions of interest are reported.

2.2. ALMA data

The $N_2H^+(1-0)$ images here analysed were first presented by Barnes et al. (2021) and were obtained as part of a high-resolution Atacama Large Millimeter/sub-Millimeter Array (ALMA) survey (project codes 2017.1.00687.S and 2018.1.00850.S, PI: A.T. Barnes) to investigate star formation in the sample of ten IRDCs first presented by Butler & Tan (2012). As reported by the authors, the observations were performed using the ALMA Band 3 receiver (frequency $\sim$93 GHz) with velocity resolution 0.1 km s^{-1} and channel width 0.05 km s^{-1}. For the observations, the 12 m array in configuration C43-1 was used together with the 7 m ACA array and the Total Power single-dish. Images from the three configurations were combined using the task FEATHER in CASA. From the final combined data cube, we extracted spectra towards Clump, Ridge, and Shock regions using a circular aperture comparable with the IRAM-30 m beam size at the $N_2H^+(1-0)$ frequency ($\sim$30″). We thus compared these spectra with the $N_2H^+(1-0)$ spectra obtained with IRAM-30 m. The three sets of spectra are comparable within the rms, indicating that all flux is recovered in the ALMA images within the uncertainty. For a more detailed description of the ALMA set-up and reduction process, we refer to Barnes et al. (2021). The final images are the same ones used by the authors, and have synthesised beam size of 3.05″×3.5″ p.a=–74° and rms 0.2 K. To increase the signal-to-noise ratio of the map, we smoothed the cube to have velocity resolution 0.2 km s^{-1}.

2.3. Mass surface density map

For this work we also used the mass surface density (Σ) map obtained towards G034.77-00.55 by Kainulainen & Tan (2013). Building on the MIREX method presented by Butler & Tan (2012), the authors combined mid- and near-infrared *Spitzer* images at multiple wavelengths to estimate the mass surface

density across the ten IRDCs in the sample from Butler & Tan (2012). For a detailed description of the MIREX method, we refer to Butler & Tan (2012) and Kainulainen & Tan (2013). The mass surface density map has an angular resolution of 2″, dictated by the resolution of the *Spitzer*-IRAC maps, and an uncertainty of ∼30%. The MIREX method is unable to estimate the mass surface density towards sources that are bright at mid-IR wavelengths, hence the pixels towards which the method fails appear as blank in the map. The Σ map is shown in Fig. 1 (right panel), with superimposed the SiO emission contours obtained in Cosentino et al. (2019) and indicated the Ridge, Shock, and Clump positions.

3. D/H at the W44-G034.77 shock interface: A multi-line approach

In Cosentino et al. (2023), we used the software MADCUBA[1] (Martín et al. 2019) to obtain local thermodynamic equilibrium (LTE) models of the $N_2H^+(1–0)$ and $N_2D^+(1–0)$ hyper-fine structures observed with the IRAM-30 m. In MADCUBA we used the spectral line identification and LTE modelling (SLIM) tool to identify the molecular transitions. Hence, we used the built-in AUTOFIT function of SLIM to obtain the LTE models that best reproduce all transitions. AUTOFIT produces the synthetic spectrum that best matches the data, assuming as input parameters the total molecular column density (N_{tot}), the radial systemic velocity of the source (v), the line full width at half maximum (FWHM), the excitation temperature (T_{ex}), and the angular size of the emission (θ_S). AUTOFIT assumes that v, FWHM, θ_S, and T_{ex} are the same for all transitions that are fitted simultaneously. We set the angular size of the emission (θ_S) to reflect the assumption that the emission fills the beam (i.e. filling factor of 1). As we show, this assumption holds for $N_2H^+(1–0)$ towards the Clump and Ridge, but may not be the case for the Shock position. However, with the current data in hand we cannot assess this for the additional transitions or species. We thus maintain the assumption of emission filling the beam for all transitions.

In Cosentino et al. (2023), we assumed T_{ex} and used MADCUBA to obtain the N_2H^+ and N_2D^+ column densities, $N(N_2H^+)$ and $N(N_2D^+)$, towards the different regions. Hence, we estimated the deuterium fractionation as

$$D_{frac}^{N_2H^+} = \frac{N(N_2D^+)}{N(N_2H^+)}. \tag{1}$$

Towards the three positions we found $D_{frac}^{N_2H^+} \sim 0.05–0.1$, a value that is enhanced by a factor of ∼2–3 with respect to the $D_{frac}^{N_2H^+}$ 3 σ upper limit (<0.03) estimated towards the Ambient region (i.e. the unperturbed gas where neither shock nor star formation activity is present).

Since a single rotational line was available, we assumed excitation temperature T_{ex}=9 K for both species and treated this as a fixed parameter in MADCUBA. This value was obtained by Cosentino et al. (2018) from the LTE analysis of multiple CH_3OH transitions at 3 mm towards G034.77. We now complement the IRAM-30 m data with APEX single pointing observations of the N_2H^+ and N_2D^+ J=3→2 transitions, towards Clump, Ridge, and Shock.

From the advantage of a multi-transitions approach, we consider the species excitation temperatures as free parameters and

use MADCUBA to obtain the best LTE models that simultaneously reproduce the J=1–0 and J=3–2 transitions. The J=1–0 spectra from Cosentino et al. (2023), the new J=3–2 spectra, and the best MADCUBA LTE models are shown in Fig. 2. The best model parameters are also reported in Table 2, together with the values already obtained in Cosentino et al. (2023). The uncertainties given by MADCUBA are <10% for T_{ex} and ∼2% for v_0 and Δv. The final uncertainty on the last two quantities is obtained by summing in quadrature the MADCUBA error with the spectra channel width (0.6–0.8 km s⁻¹ or ∼10%). Finally, the uncertainty on $D_{frac}^{N_2H^+}$ is obtained by adding in quadrature the uncertainties on $N(N_2H^+)$ and $N(N_2D^+)$.

From Table 2, the T_{ex} here obtained are a factor of 2 lower that that assumed in Cosentino et al. (2023), but consistent between the two species. As a consequence, the column densities and therefore the $D_{frac}^{N_2H^+}$ here obtained are in agreement with those inferred in Cosentino et al. (2023). The 3σ D/H upper limit previously estimated for the Ambient region does not change significantly when T_{ex}=4.5 K is assumed. For all species and towards all positions the optical depth τ is ≪ 1. The multi-transition approach here adopted confirms the results reported in Cosentino et al. (2023) and its implications. In particular, the $D_{frac}^{N_2H^+}$ values across the shock front between W44 and G034.77 are consistent with those typically measured in dense and cold material with a high potential to yield star formation, for example both low- and high-mass pre-stellar and starless cores (Emprechtinger et al. 2009; Fontani et al. 2011; Friesen et al. 2013; Kong et al. 2016; Punanova et al. 2016).

4. N₂H⁺ kinematics and morphology: Fragmented versus continuous material

We now use the high angular resolution ALMA images of the $N_2H^+(1–0)$ emission towards G034.77 (Barnes et al. 2021; Fontani et al. 2021) to investigate the morphology and kinematics of the dense gas in the proximity of the shock front. The N_2H^+ integrated intensity map (39–45.5 km s⁻¹; top panel) is shown in Fig. 3, together with the velocity field (moment 1) map (bottom panel). In both panels, the SiO emission contours are overlaid (black contours) and the pixels below 3×A_{rms}[2] have been masked. The Σ_{H_2}=0.09 g cm⁻² (visual extinction 20 mag) (Kainulainen & Tan 2013) contour (magenta) highlights the shape of the cloud. We note that all the integrated intensity maps presented in this work were obtained considering only the emission from the isolated component of the N_2H^+ hyper-fine structure, which is optically thin.

As shown in Fig. 3, the dense gas is spatially distributed across the ridge and further in, within the cloud, but it is not widespread everywhere towards the source. The emission is indeed mostly distributed along two parallel elongations that notably are also parallel to the direction of the shock front probed by the SiO emission. Both elongations show multiple emission peaks, the brightest of which is located in correspondence with the region named the Clump in Cosentino et al. (2023). From the velocity field map (right panel), the dense gas emission across the ridge appears as a velocity-coherent component at ∼39–41 km s⁻¹. On the other hand, the elongation within the cloud appears as the superposition along the line of sight of at least two velocity-coherent components: a central more compact structure

---

[1] MADCUBA is a software developed in the Madrid Center of Astrobiology (INTA-CSIC). https://cab.inta-csic.es/madcuba/

[2] A_{rms}=rms×dv × $\sqrt{N_{channels}}$, where rms is the spectra noise, dv is the spectral resolution in km s⁻¹, and $N_{channels}$ is the number of channels that have been integrated.
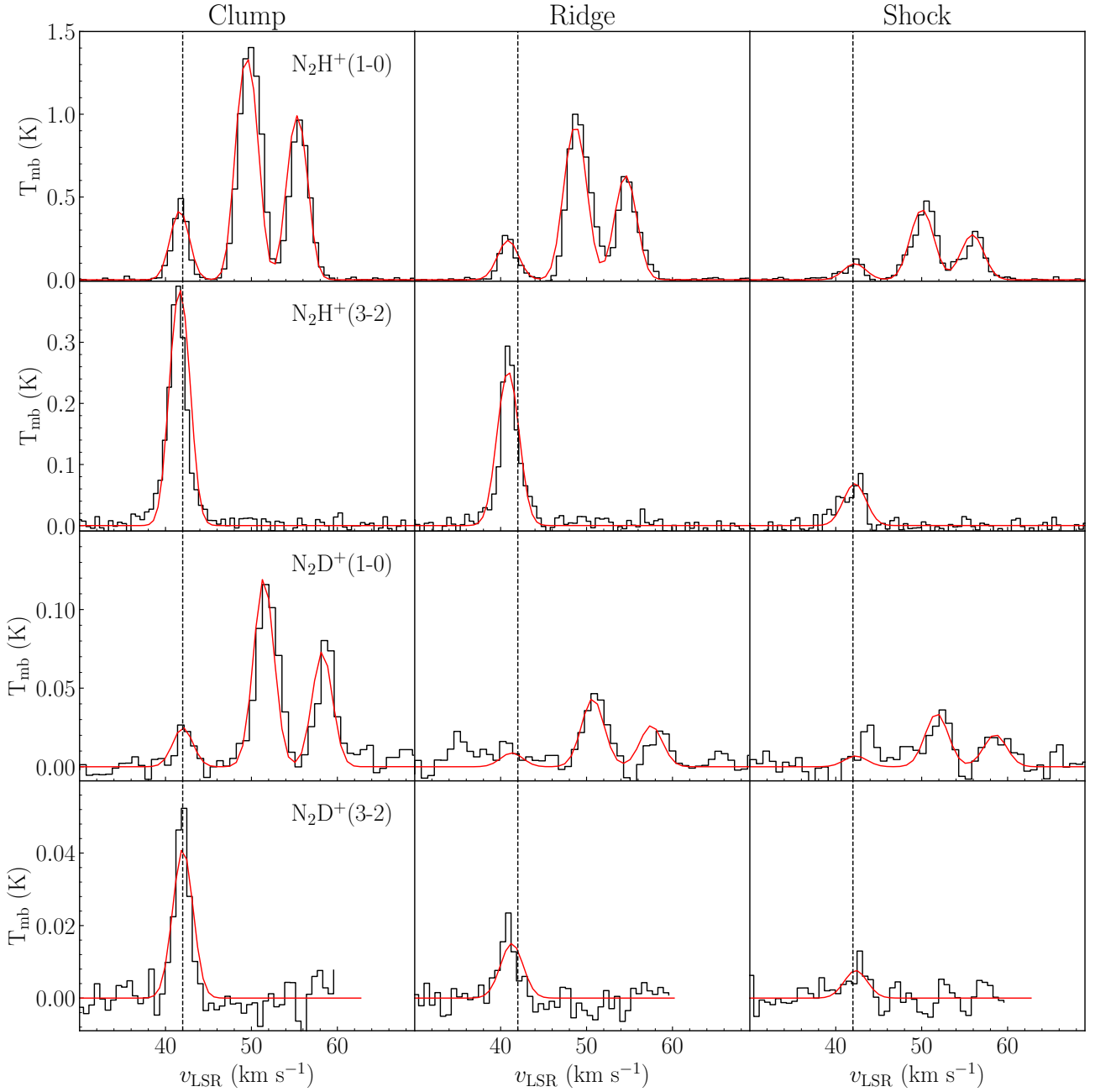
Fig. 2. N$_2$H$^+$ (first and third rows) and N$_2$D$^+$ (second and fourth rows) spectra of the J=1–0 and J=3–2 transitions obtained towards the Clump, Ridge, and Shock. The IRDC G34.77 central velocity is indicated as a vertical dotted line in all panels. The red curves show the best LTE models obtained by MADCUBA.

Table 2. N$_2$H$^+$ and N$_2$D$^+$ best LTE model parameters, as obtained by MADCUBA (odd lines), towards the three positions and corresponding $D_{\mathrm{frac}}^{\mathrm{N_2H^+}}$.

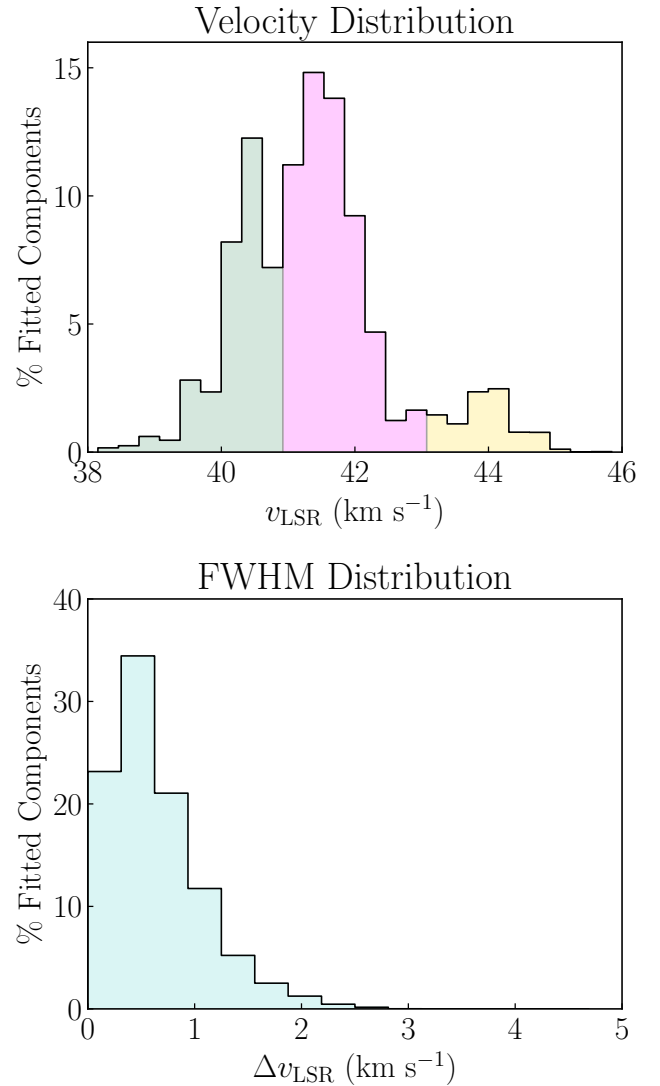|	N$_2$H$^+$				N$_2$D$^+$					
	N_{tot} (10^{13} cm^{-2})	T_{ex} (K)	v_0 (km s^{-1})	Δv (km s^{-1})	N_{tot} (10^{12} cm^{-2})	T_{ex} (K)	v_0 (km s^{-1})	Δv (km s^{-1})	$D_{\mathrm{frac}}^{\mathrm{N_2H^+}}$	Reference
Shock	0.50±0.04	4.4	42.2	3.0	0.5±0.1	3.9	42.3	3.1	0.080±0.006	This work
	0.36±0.09	9	42.2	3.2	0.3±0.1	9	42.2	3.2	0.07±0.03	Cosentino+23
Ridge	1.10±0.05	4.9	40.9	2.8	0.6±0.07	4.4	41.3	3.1	0.055±0.007	This work
	0.8±0.2	9	40.9	3.1	0.4±0.1	9	41.4	3.1	0.05±0.03	Cosentino+23
Clump	1.70±0.08	4.8	41.7	2.5	1.4±0.08	4.3	42.0	2.7	0.10±0.02	This work
	1.1±0.1	9	41.7	2.8	1.2±0.1	9	42.1	3.0	0.10±0.02	Cosentino+23

Notes. For each position we also report the corresponding values already presented in Cosentino et al. (2023) (Cosentino+23; even lines).
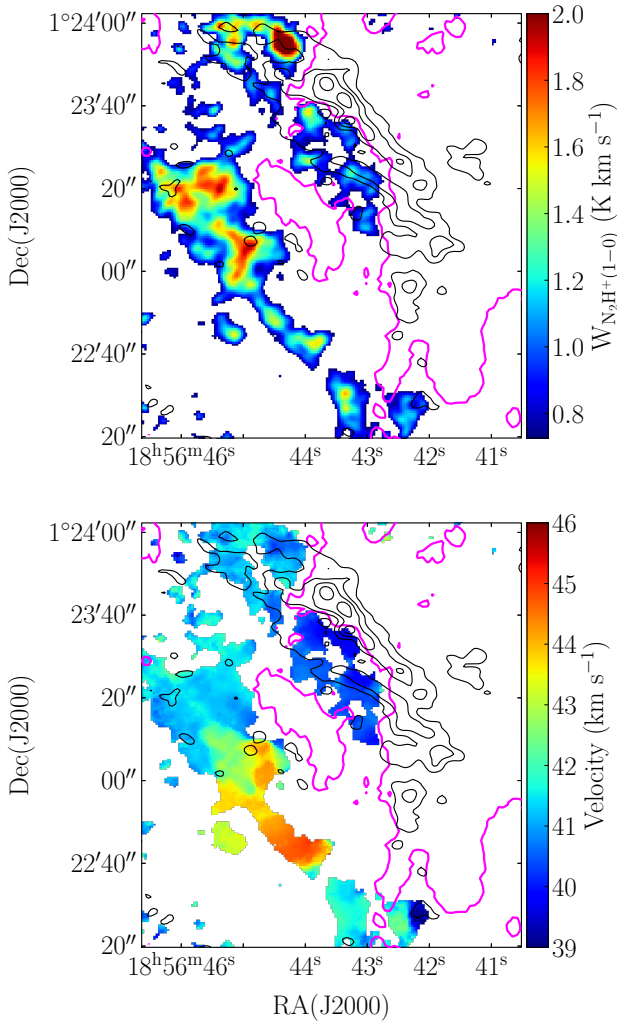
Fig. 3. Integrated intensity map (top panel) and velocity field map (bottom panel) of the $N_2H^+(1-0)$ emission towards the shock front in G034.77. In both panels, the pixels below $3\times A_{rms}$ have been masked (Arms= 0.23 K km s^{-1}). The Σ_{H_2}=0.09 g cm^{-2} (visual extinction 20 mag) magenta contour highlights the shape of the cloud (Kainulainen & Tan 2013). The SiO(2–1) emission contours obtained by Cosentino et al. (2019) is shown as black contours from 3σ (σ=0.016 Jy beam^{-1} km s^{-1}) by steps of 3σ.

Fig. 4. Velocity (top panel) and FWHM (bottom panel) distributions of the $N_2H^+(1-0)$ emission towards G034.77. The bin sizes are 0.3 km s^{-1}, which corresponds to one-third of mean intensity-weighted linewidth.

with velocity ∼43–45 km s^{-1} and a more widespread, elongated emission at ∼41–42 km s^{-1}.

To more accurately constrain these components, we used the semi-automated PYTHON tool SCOUSEPY (Henshaw et al. 2016) to perform multi-Gaussian fitting of all the spectra in the data cube. The SCOUSEPY output provides information on the velocity, intensity, and FWHM of the multiple velocity components towards each positional element in a data cube. We obtained this information for the N_2H^+ emission mapped with ALMA (∼30 000 spectra fitted) and used it to build velocity (top panel) and FWHM (bottom) distributions for the dense gas emission in G034.77. For a detailed description of SCOUSEPY, we refer to Henshaw et al. (2016) and Henshaw et al. (2019). For the SCOUSEPY analysis of the ALMA N_2H^+ emission, we re-binned the data to have a velocity channel 0.2 km s^{-1} and considered only the isolated component of the $N_2H^+(1-0)$ hyper-fine structure. The velocity and FWHM distributions built from the SCOUSEPY output are shown in Fig. 4. From the FWHM distribution, the dense gas emission is overall relatively narrow (mean

intensity weighted FWHM = 0.9 km s^{-1}), with line widths narrower than 2 km s^{-1}. As already hinted by the velocity field map, the velocity distribution in Fig. 4 indicates the presence of multiple velocity components in the dense gas: (i) a component spatially associated with the dense ridge, with velocities between ∼38–41 km s^{-1}; (ii) a component located within the inner cloud, with velocities in the range ∼41–43 km s^{-1}; and (iii) a third higher-velocity component (∼43–45 km s^{-1}) also located within the cloud, but showing a more compact morphology. To better identify the spatial distribution of each velocity component, we obtained integrated intensity maps towards the three velocity ranges mentioned above, as shown in Fig. 5.

In Fig. 5, the three components are very spatially separated. The lower velocity component (38–41 km s^{-1}) is mostly located towards the dense ridge and closely follows its shape, while the other two components are located towards the inner cloud. A partial overlap of the 38–41 km s^{-1} and 41–43 km s^{-1} components is found towards the north and east of the cloud (with east being the direction of increasing RA(J2000)), where the region labelled Clump is located. Finally, the spatial distribution of the velocity component at 43–45.5 km s^{-1} appears as complementary to the
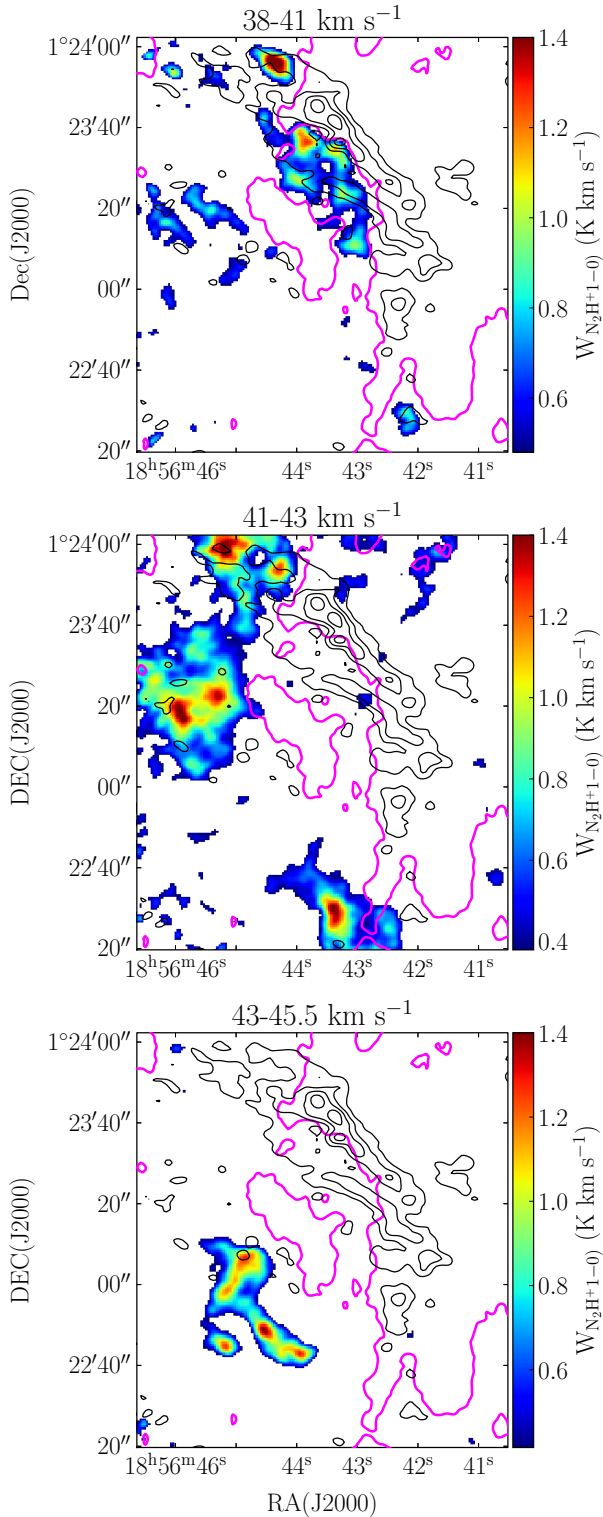
Fig. 5. Integrated intensity maps of the N$_2$H$^+$(1–0) emission for the three identified velocity components, i.e. 38–41 km s^{-1} (top panel; A$_{rms}$=0.16 K), 41–43 km s^{-1} (middle panel; A$_{rms}$=0.13 K), and 43–45.5 km s^{-1} (bottom panel; A$_{rms}$=0.14 K). In all panels, the pixels below 3×A$_{rms}$ have been masked. The Σ_{H_2}=0.09 g cm^{-2} (visual extinction 20 mag) magenta contour highlights the shape of the cloud (Kainulainen & Tan 2013). The SiO(2–1) emission (Cosentino et al. 2019) is shown as black contours from 3σ (σ=0.016 Jy beam^{-1} km s^{-1}) in steps of 3σ.

41–43 km s^{-1} component and is relatively compact and spatially corresponding to a bright feature (i.e. density enhancement) in the Σ map. In Fig. 5 all three components show several peaks in the N$_2$H$^+$ emission. However, while all the emission peaks at 41–45.5 km s^{-1} lie on top of a more extended and fainter emission, the emission peaks at velocities 38–41 km s^{-1} appear as little fragments or core-like structures almost detached from each other. We now investigate the nature of these fragments, and infer their physical and dynamical properties.

5. Shock induced star formation in G034.77

5.1. Core identification

To systematically constrain the position and extent of the fragment-like structures, we now perform a dendogram analysis (Rosolowsky et al. 2008) on the full (38–45.5 km s^{-1}) N$_2$H$^+$ integrated intensity map. Dendograms provide a robust and consistent method for the identification of hierarchical structures within maps and cubes. The smallest of these structures are called leaves and are widely considered good identifier of core-like objects. We built dendogram using the PYTHON package ASTRODENDRO[3], which requires the user to define a set of parameters. These are MIN_VALUE (the minimum intensity to be considered by the algorithm), MIN_DELTA (the minimum intensity difference between isocontours), and MIN_PIX (the minimum number of pixels within a structure). Following the analysis of Barnes et al. (2021) and the method adopted in several previous works (Cheng et al. 2018; Liu et al. 2018; O'Neill et al. 2021), we set min_value=3σ = 0.70 K km s^{-1}, min_delta= 1σ = 0.23 K km s^{-1}, and MIN_PIX= 0.5 beam = 18 pixels and perform the analysis on the non-primary beam corrected image. However, since most of the region of interest is located towards the centre of the map, the analysis performed on the primary beam corrected image is not significantly different. From the dendogram analysis of the N$_2$H$^+$ integrated intensity map we identified 41 leaves. From this list, we excluded all those leaves for which the extracted spectra show no significant emission (i.e. they are artefacts due to noise effects and are mostly located at the edge of the map). The final number of significant leaves is 26, and we refer to them as cores. In Table 3, we report the physical and dynamical properties obtained for the cores here identified. In Fig. 6 we show the 26 cores overlaid on the mass surface density (Σ).

In Fig. 6, several cores are identified throughout the source, and especially within the ridge. The mass surface density peak located in correspondence with the Clump region is also clearly seen, together with two additional cores nearby. The majority of the identified cores are spatially associated with well-defined peaks in the mass surface density map (Fig. 6). This is particularly clear towards the ridge, where the emission is not saturated due to the bulk of the Σ emission from the main cloud. From the Σ map, we estimated the core mass surface densities as the average Σ value within the corresponding leaf and convert this to mass by multiplying by the leaf area. We obtain masses in the range 1–20 M$_\odot$. In particular, the cores in correspondence with the Clump region have a mass of ~10 M$_\odot$. Since the MIREX method used to obtain the Σ map is known to slightly underestimate the mass surface density in bright continuum regions (Kainulainen & Tan 2013), the obtained masses are likely lower limits. Assuming spherical geometry for the cores, we estimated

---

[3] https://dendrograms.readthedocs.io/en/stable/

Table 3. Properties of the identified cores.

Idx	x_{core} (deg)	y_{core} (deg)	Σ (g cm^{-2})	Mass (M$_\odot$)	r (pc)	σ_{tot} (km s^{-1})	n_{H_2} (10^5 cm^{-3})	t_{ff} (10^4 yr)	M$_J$ (M$_\odot$)	λ_J (pc)	α_{vir}	B (mG)
1	284.189	1.369	0.07	3.4	0.031	0.6	3.6	5.2	0.9	0.042	3.9	0.6
4	284.176	1.374	0.01	4.6	0.029	0.7	6.0	4.0	0.7	0.032	3.4	0.8
5	284.181	1.375	0.11	8.1	0.033	0.6	6.8	3.7	0.7	0.030	1.9	0.7
10	284.183	1.379	0.14	5.1	0.025	0.3	9.7	3.1	0.6	0.025	0.5	0.5
11	284.198	1.380	0.15	11.2	0.036	0.7	7.5	3.6	0.6	0.029	1.7	0.7
12	284.188	1.379	0.14	4.0	0.021	0.2	14.1	2.6	0.5	0.021	0.3	0.7
13	284.186	1.380	0.12	3.3	0.021	0.4	11.2	2.9	0.5	0.024	1.0	0.1
16	284.188	1.385	0.16	20.2	0.052	0.4	4.3	4.7	0.9	0.038	0.6	0.4
18	284.190	1.385	0.15	3.1	0.019	0.5	14.1	2.6	0.5	0.021	1.9	0.8
19	284.179	1.387	0.07	1.6	0.019	0.6	7.4	3.6	0.7	0.029	4.8	0.8
20	284.192	1.388	0.13	3.2	0.022	0.5	9.7	3.1	0.6	0.025	1.6	0.5
22	284.190	1.389	0.16	6.7	0.027	0.5	10.5	3.0	0.5	0.024	1.2	0.4
23	284.180	1.390	0.09	4.2	0.028	0.7	5.7	4.1	0.7	0.033	3.6	0.8
25	284.183	1.391	0.08	2.5	0.022	0.5	7.5	3.6	0.6	0.029	2.3	0.6
26	284.194	1.392	0.08	0.8	0.013	0.3	10.5	3.0	0.5	0.024	1.7	0.4
29	284.181	1.393	0.09	2.0	0.019	0.4	8.5	3.3	0.6	0.027	1.9	0.5
30	284.183	1.393	0.09	3.5	0.025	0.6	6.6	3.8	0.7	0.031	3.2	0.8
32	284.190	1.394	0.10	1.1	0.014	0.6	11.5	2.9	0.5	0.023	6.0	1.1
33	284.186	1.395	0.12	4.1	0.026	0.7	7.2	3.6	0.7	0.029	4.0	1.0
35	284.185	1.399	0.14	6.4	0.026	0.6	11.7	2.9	0.5	0.023	1.8	0.8
36	284.188	1.400	0.15	6.7	0.033	0.3	5.6	4.1	0.7	0.033	0.7	0.3
37	284.190	1.402	0.17	6.0	0.025	0.6	11.7	2.8	0.5	0.023	1.6	0.7
38	284.186	1.402	0.13	3.8	0.021	0.3	12.8	2.7	0.5	0.022	0.7	0.4
39	284.185	1.402	0.11	0.6	0.009	0.3	24.2	2.0	0.4	0.016	1.5	0.5
40	284.178	1.402	0.09	2.5	0.022	0.3	7.0	3.7	0.7	0.030	1.1	0.1
41	284.184	1.403	0.08	1.1	0.016	0.3	7.8	3.5	0.6	0.028	1.9	0.4
42	284.182	1.403	0.08	1.1	0.014	0.3	11.4	2.9	0.5	0.023	1.9	0.5

Notes. The columns list (from left to right) the index assigned by ASTRODENDRO, equatorial coordinates of the core centre, core mass surface density, mass, radius, total velocity dispersion from the N$_2$H$^+$ spectra, hydrogen volume density, free-fall time, Jeans mass and length, virial parameter, and minimum magnetic field strength to prevent the core collapse.
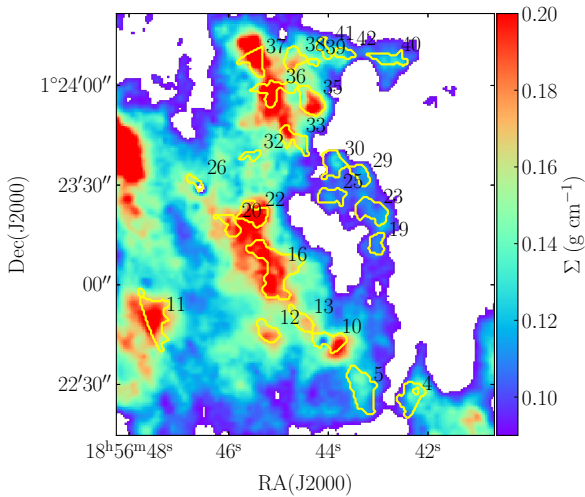
Fig. 6. Position of the cores (yellow) identified by the dendogram analysis and overlaid mass surface density map from Kainulainen & Tan (2013) (color scale). Pixels below a threshold of σ=0.09 g cm^{-2} have been masked.

their volume density as

$$n_{H_2} = \frac{M}{\frac{4}{3}\pi r^3 \mu_{H_2} m_H}, \tag{2}$$

where μ_{H_2}=2.8 is the mean molecular weight per hydrogen molecule, m_H is the mass of the hydrogen atom, and r is the effective radius of the core. We find volume densities in the range $(4–20)\times10^5$ cm^{-3}. The corresponding free-fall times are in the range $(2–5)\times10^4$ yr and were estimated as

$$t_{ff} = \left(\frac{\pi^2 r^3}{8GM}\right)^{0.5}, \tag{3}$$

where G is the gravitational constant.

5.2. Core stability against thermal, turbulent and magnetic support.

To investigate whether cores are stable against thermal support, we estimate their Jeans masses and lengths as follows:

$$M_J = \frac{\pi^{5/2} c_s^3}{6 G^{3/2} \rho^{1/2}}, \tag{4}$$

$$\lambda_J = c_s \left(\frac{\pi}{G\rho}\right)^{1/2}. \tag{5}$$

Here, ρ is the core volume mass density and c_s is the sound speed, defined as

$$c_s = \sqrt{\frac{k_b T_{kin}}{m_H \mu_p}}. \tag{6}$$

We assume $T_{kin} = 15$ K, consistently with Cosentino et al. (2019), and the mean molecular mass $\mu_p = 2.37$, for a typical interstellar elemental abundance. We find M_J in the range 0.3–0.7 $M_\odot$ and $\lambda_J \sim 0.03$ pc for all cores. We find that $M/M_J > 2$ and up to 20 for all 16 cores. We also investigate the spatial distribution of the cores by calculating their minimum separation. For this we use the PYTHON package NETWORKX[4] to calculate the cores' minimum spanning tree (MST), which is the minimum set of edges connecting the core centre positions. We obtain that the minimum separation between cores is in the range 0.07–0.5 pc (average ~0.2 pc), which is comparable to the Jeans length calculated for the ridge and the inner cloud and larger than the core Jeans length. This indicates that, if not further supported, for instance by turbulence and/or magnetic field, the cores are unstable against thermal support.

We now test the core stability, considering both thermal and turbulent support in the form of kinetic energy E_{kin} against gravity, in the form of potential energy E_{pot}. The balance between these two terms lead to the virial parameter α_{vir} (Bertoldi & McKee 1992). In the idealised case of a spherical core of uniform density supported by only kinetic energy (i.e. neglecting magnetic fields), the virial parameter takes the form

$$\alpha_{vir} = a\frac{5\sigma_{tot}^2 r}{GM}, \qquad (7)$$

where σ_{tot} is the N_2H^+ velocity dispersion including both thermal and non-thermal broadening (Fuller & Myers 1992; see also Eq. (6) in Barnes et al. 2023). We note that Eq. (7) does not take into account contributions due to in-falling and/or out-flowing material. The factor a accounts for systems with non-spherical and non-homogeneous density distributions, and for most of these a value $a = 2\pm 1$ is assumed (Bertoldi & McKee 1992). Hence, cores with $\alpha_{vir} < 2$ are considered bound and unstable against collapse, while cores with $\alpha_{vir} > 2$ will likely be dispersed. We find that 20 out of 26 cores have $\alpha_{vir} < 2$, 4 cores have $\alpha_{vir} \leq 4$, and 2 cores have $\alpha_{vir} > 4$. Hence, 20 out of 26 cores are unstable to collapse when only supported by thermal and turbulent pressure. However, the uncertainty on α_{vir} accounts for ~40%, with the major contribution due to the mass surface density uncertainty. Therefore, $\alpha_{vir} \leq 4$ is also consistent with the bound core scenario, within the uncertainties.

We also tested the core stability when support from magnetic field is included. In this case, the virial parameter takes the following form (Pillai et al. 2011):

$$\alpha_{B,vir} = a\frac{5r}{GM}\left(\sigma_{tot}^2 - \frac{v_A^2}{6}\right). \qquad (8)$$

Here the Alfvén velocity is $v_A = B(v_0 \rho)$, with B being the magnetic field strength and v_0 the permeability of free space. As for the previous case, no in-falling or out-falling material is taken into account. Hence, by setting $a = 2\pm 1$ and solving the equation for B, we infer that the required magnetic field pressure to support the cores against collapse is in the range 0.1–1 mG. For comparison, the magnetic field strength reported in the literature are of a few milligauss in high-mass star-forming regions (e.g. Beltrán et al. 2019; Dall'Olio et al. 2019), in the range 0.2–5 mG (e.g. the BISTRO survey; Kwon et al. 2018) towards low-mass star-forming regions and ~0.5 mG in IRDCs (Pillai et al. 2015; Soam et al. 2019). These values are sufficient to support the cores against collapse.


[4] https://pypi.org/project/networkx/
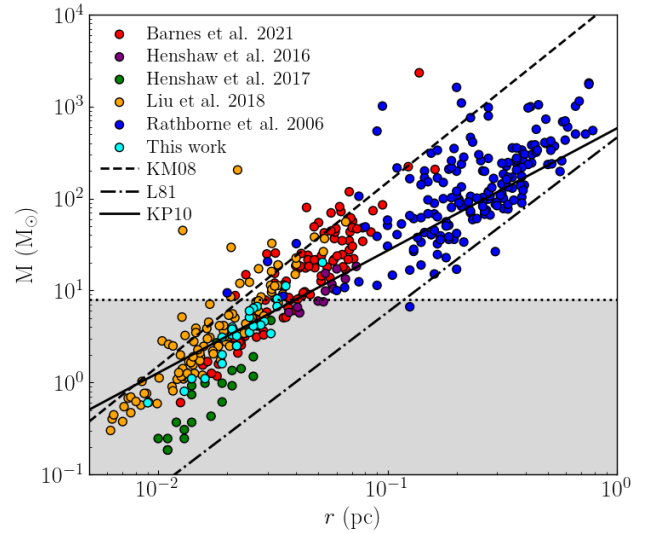
Fig. 7. Core masses as a function of sizes for the cores identified in this this work (cyan dots). For comparison, the mass and the sizes of the cores and/or clumps determined by Rathborne et al. (2006); Henshaw et al. (2016, 2017); Liu et al. (2018); Barnes et al. (2021) and homogenised by Barnes et al. (2021) are reported as coloured dots. Overlaid as the diagonal black lines are the mass–radius relations taken from (Larson 1981, L81; dash-dotted line), the high-mass star formation thresholds taken from (Krumholz & McKee 2008, KM08; dashed line) and (Kauffmann et al. 2010, KP10; solid line). The KP10 relation has been scaled by a factor of 1.5 to match the dust opacity used in Barnes et al. (2021). The horizontal dotted black line shows the mass threshold of high-mass stars (>8 $M_\odot$).

The IRDC G034.77 has been extensively studied as part of a larger sample. In Rathborne et al. (2006), the source was part of a sample of 38 IRDCs, while in more recent works (Henshaw et al. 2016, 2017; Liu et al. 2018; Barnes et al. 2021) the cloud is part of a sample of ten IRDCs first presented by Butler & Tan (2009, 2012). In Fig. 7, we compare the core mass-size relation here estimated with those reported by these authors in the larger samples and estimated from 1 and 3 mm continuum observations. For this we used the homogenised sample presented by Barnes et al. (2021) that was obtained by standardising the parameters used to determine the physical properties of the cores and clumps.

In Fig. 7, the cores identified in this work closely follow the mass-size trend of the homogenised sample. The cores mostly lie on the low-mass end with just two exceptions, and sit above or below the KP10 relation. Hence, if the cores harbour star formation, this may result in a population of low-mass stars. The few exceptions to this are cores 11 and 16, which are the most extended ($r \sim 0.04$–0.05 pc) and massive (11 and 20 $M_\odot$) in our sample and have a virial parameter < 2. Hence, these cores have the potential to host high-mass star formation assuming that no further fragmentation occurs and that the magnetic field is not strong enough to prevent their collapse. The mass-size relation of the G034.77 cores is in rough agreement (within the uncertainty) with the relation estimated by Kauffmann et al. (2010). In Fig. 8, we also compare the relation between the virial parameter and the core masses from this work with that inferred by Barnes et al. (2021). In Fig. 8, it can be seen that the two trends are in close agreement and largely overlap. In light of these comparisons, the properties of the cores here estimated closely follow the trends estimated from a sample of sources that have similar
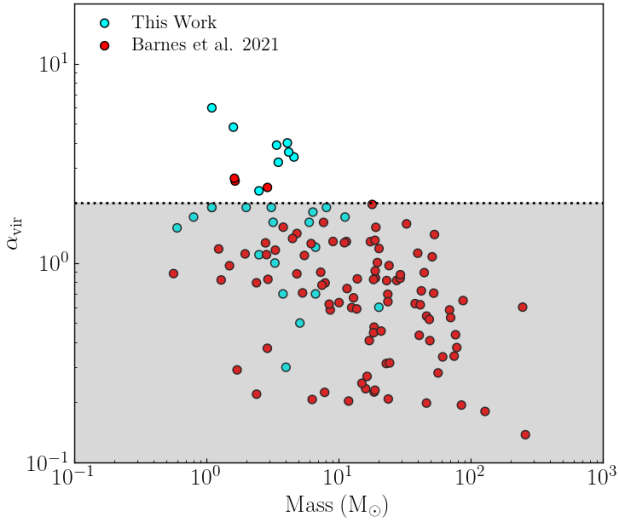
Fig. 8. Core virial parameters as a function of core masses for the cores identified in this work (cyan dots) and compared with the results from Barnes et al. (2021) (red dots). The horizontal dotted black line and the grey area shows the virial parameter threshold for bound cores.

masses, distances, and contrast against the mid-IR Galactic background to G034.77 (Butler & Tan 2009, 2012).

6. Discussion and conclusions

The mechanisms responsible for the ignition of star formation in molecular clouds are still under debate. Among several possible scenarios, it has been proposed that large-scale interstellar shocks driven by stellar feedback, such as SNRs, may regulate star formation in galaxies (e.g. Inutsuka et al. 2015; Khullar et al. 2024). By means of the interplay between positive and negative feedback, interstellar shocks may be able to set the low levels of star formation efficiency typically measured in nearby galaxies. Several theoretical predictions have been proposed for this scenario, but poor observational constraints are available in the literature. In particular, it is unclear whether SNRs can trigger star formation in impacted molecular clouds. In this work, we studied the morphology and kinematics of the typical dense gas tracer N_2H^+ towards the IRDC G034.77, which is shock-interacting with the SNR W44. The N_2H^+ emission is known to probe very dense and cold gas (critical density 10^5 cm^{-3}; Jørgensen et al. 2004) and is often used to identify cores in molecular clouds.

According to the analysis presented in this work, the N_2H^+ emission is not widespread across the source, but is mostly organised in two elongated structures, one mainly distributed towards the Ridge and the Clump region and the other located further in (towards the east) within the cloud. From the SCOUSEPY analysis, the elongation towards the ridge has a velocity in the range 38–41 km s^{-1}, while the eastern elongation splits into two spatially separated velocity components at 41–43 and 43–45.5 km s^{-1}. This higher-velocity component is consistent with the cloud systemic velocity, 43.5 km s^{-1} reported by Simon et al. (2006), Rathborne et al. (2006) and Hernandez & Tan (2015). Moreover, the more accurate SCOUSEPY analysis shows that the low- and mid-velocity components spatially overlap towards the north-east of the cloud (i.e. where the Clump is located) and kinetically connected not just towards the Clump, but also marginally towards the centre of the innermost

elongation. The velocities of these two components are consistent with the minimum velocities achieved in the J- and C-type shocks. From the SiO map presented in Cosentino et al. (2019), the shock is approaching the ridge at a velocity of ~46 km s^{-1}, and decelerates to 39 km s^{-1} while plunging into the ridge. This kinematics is consistent with a CJ-type MHD shock, where the J-type component has a velocity of 46–42 km s^{-1} and the C-type component has a velocity 42–39 km s^{-1}. Hence, we speculate that the shock interaction driven by W44 may have penetrated within the cloud further than is shown by the SiO emission. SiO emission is known to trace shocked gas that is very dense (critical density >10^5 cm^{-3}; Schilke et al. 1997), and more in general it is a good probe of the most powerful parts of the shock. In our proposed scenario, the SiO emission only probed 'the tip of the iceberg' (i.e. the most powerful part of a more extended shock). In line with this, since the strongest shock is occurring towards the ridge, the gas there is decelerated to lower velocities compared to the material within the inner cloud. Here, the much higher mass surface density (more than a factor of 2) may have prevented the gas from being decelerated as strongly as towards the ridge and helped the shock to be dissipated more quickly (Shima et al. 2017). Finally, at this higher density the SiO freeze-out time is shorter than that at the ridge density (Martin-Pintado et al. 1992; Jiménez-Serra et al. 2005). A supporting factor to this scenario is the fact that both the ridge and the innermost elongation stand out as almost isolated features in the mass surface density map and have orientations similar to that of the SiO shock front. In particular, while the ridge appears as a spatially independent feature, the innermost elongation correspond to a large overdensity within the cloud.

While no data are available to estimate the D/H ratio for the innermost emission, we have confirmed that the N_2H^+ deuteration towards the ridge is significantly enhanced with respect to that measured towards the Ambient position. In Cosentino et al. (2023), we identified this position as probing the bulk of the cloud and as being far away from the shock front and devoid of clear signatures of ongoing star formation. However, from the high-resolution N_2H^+ image here investigated, the Ambient position is located in the vicinity of core 11 and not too far away from the high-velocity N_2H^+ component. Hence, in the light of the new results, we cannot exclude that the Ambient position may also be affected by shocks and that these effects are not detectable within the relatively large beam of the single-dish observations. High-resolution N_2D^+ images are needed to further investigate this. With the data currently in hand, the Ambient position seems not to be associated with bright N_2H^+ emission nor with mass surface density peaks, as shown in Figs. 3 and 6. This, together with the lack of $N_2D^+(1–0)$ emission reported in Cosentino et al. (2023), hints at the idea that the gas across the ridge is denser and colder than that towards the Ambient position. High D/H ratios are known to be positively correlated with CO depletion (e.g. Miettinen & Offner 2013; Punanova et al. 2016; Barnes et al. 2016), which occurs for gas temperatures below 20 K (Caselli et al. 1999). We will present a detailed investigation of the CO depletion in G034.77 in a series of forthcoming works (Petrova et al., in prep.; Segev et al., in prep.), using multiple CO transitions mapped with both the Green Bank 100 m antenna and ALMA. However, these preliminary studies seem to indicate relatively high CO depletion levels towards the ridge and the inner cloud (≥4), but not the Ambient, suggesting that the shock compressed gas is indeed dense (n$_{(H_2)}$ ≥ 10^5 cm^{-3}; Cosentino et al. 2019) and cold.

In Cosentino et al. (2023), the single pointing observations did not allow us to investigate the spatial morphology of

this compressed material. Hence, we were unable to rule out whether this post-shocked gas is organised as a continuous slab of compressed material or if it has fragmented into cores. In the high-resolution ALMA images here analysed, the dense gas appears highly fragmented, especially towards the ridge, with several core-like structures. These cores are well identified in our dendogram analysis and are spatially associated with emission peaks in the mass surface density map. The cores have masses in the range 1–20 $M_\odot$ and closely follow the mass-size trend of the homogenised core sample presented by Barnes et al. (2021), which also includes results from Rathborne et al. (2006), Henshaw et al. (2016, 2017) and Liu et al. (2018) as well as literature works (Larson 1981; Sánchez-Monge et al. 2013; Peretto et al. 2013; Kauffmann et al. 2013; Kainulainen & Tan 2013; Chen et al. 2020). We suggest that these cores do not host deeply embedded protostars, but may either be in a starless or pre-stellar stage for the following reasons. Most cores appear as density enhancements in the mass surface density map from Kainulainen & Tan (2013) (see Fig. 6). Moreover, the *Herschel* 70 μm image in Fig. 1 shows no significant emission peaks associated with the cores. No molecular outflow signatures are found in our current SiO ALMA map (Cosentino et al. 2019), and this seems to be confirmed by the CO ALMA emission maps that will be presented in Segev et al. (in prep.). All this suggests that the cores do not host deeply embedded protostars, and thus the identified cores may either be in a starless or pre-stellar stage. None of the cores here identified is detected in the 1 mm and 3 mm continuum images of Rathborne et al. (2006), Barnes et al. (2021) and Cosentino et al. (2019), respectively. However, it is important to note that N_2H^+ is a resilient tracer of imminent star formation in molecular clouds (Priestley et al. 2023) and that starless cores with no millimetre continuum emission have been reported by means of N_2D^+ emission (e.g. Kong et al. 2017). Additionally, since the continuum emission is the most established method of identifying cores in molecular clouds, our current understanding of the correlation between starless core and millimetre continuum emission could be biased. Finally, we note that the detection limit of the Rathborne et al. (2006) single-dish 1.2 mm maps, due to beam size and source distances effects, is <45 $m_\odot$, well above the core masses here reported. Higher-resolution 1 mm maps are therefore needed to establish whether the cores are associated with continuum sources.

The minimum separation between cores is, on average, 0.2 pc and is consistent with the fragmentation scales of the inner cloud and the ridge. Moreover, except for a few, the cores appear unstable against gravitational collapse in the presence of thermal and turbulent pressure. We estimate that a magnetic field 0.5–1 mG may support these cores against collapse. These values are consistent with the ∼0.85 mG magnetic field indirectly estimated towards G034.77 in Cosentino et al. (2019), but this value is relatively uncertain since it was indirectly inferred from shock models.

The field of view of our N_2H^+ ALMA map does not cover the region of the cloud near the HII region where Paron et al. (2009) reported evidence of star-forming cores. These sites are associated with molecular outflows and point-like IR emission and are likely more evolved than the cores here identified. Furthermore, as reported by the authors, they are spatially aligned with the expanding HII region shells. As a consequence, the authors conclude that star formation was not triggered by the SNR, but rather by the HII region through the collect and collapse process. On the other hand, the field of view of our observations is well covered by the IR and molecular tracer maps of Paron et al. (2009), but the authors do not report evidence of relatively

evolved star formation activity in the vicinity of W44. Hence, it is unlikely that the cores here identified were produced by the HII region and/or pre-SNR stellar wind compression. This indicates that, if the cores here identified will form stars in the future, the two shock compressions (i.e. the HII region and the SNR-driven shocks) will lead to star populations at different evolutionary stages (i.e. the multi-episodic star formation often observed in molecular clouds) (e.g. Jerabkova et al. 2019).

In light of all this, we suggest a scenario in which the large-scale shock driven by SNR W44 has penetrated within the IRDC G034.77, compressing the gas along both a high-density elongation within the cloud and a lower density ridge at the edge. Within these features, the shock passage may have triggered the formation of cores at spatial scales consistent with the Jeans length. Due to the lack of deeply embedded sources and molecular outflow signatures, the cores are either in a starless or pre-stellar stage and appear stable against gravitational collapse, although the importance of the magnetic field also needs to be addressed. Further high-resolution observations of dedicated tracers are needed to confirm this scenario.

References

Abdo, A. A., Ackermann, M., Ajello, M., et al. 2010, Science, 327, 1103
Awad, Z., Viti, S., Bayet, E., & Caselli, P. 2014, MNRAS, 443, 275
Barnes, A. T., Kong, S., Tan, J. C., et al. 2016, MNRAS, 458, 1990
Barnes, A. T., Henshaw, J. D., Fontani, F., et al. 2021, MNRAS, 503, 4601
Barnes, A. T., Liu, J., Zhang, Q., et al. 2023, A&A, 675, A53
Beltrán, M. T., Padovani, M., Girart, J. M., et al. 2019, A&A, 630, A54
Bertoldi, F., & McKee, C. F. 1992, ApJ, 395, 140
Butler, M. J., & Tan, J. C. 2009, ApJ, 696, 484
Butler, M. J., & Tan, J. C. 2012, ApJ, 754, 5
Cardillo, M., Tavani, M., Giuliani, A., et al. 2014, A&A, 565, A74
Caselli, P., Walmsley, C. M., Tafalla, M., Dore, L., & Myers, P. C. 1999, ApJ, 523, L165
Caselli, P., Benson, P. J., Myers, P. C., & Tafalla, M. 2002, ApJ, 572, 238
Caselli, P., Vastel, C., Ceccarelli, C., et al. 2008, A&A, 492, 703
Castelletti, G., Dubner, G., Brogan, C., & Kassim, N. E. 2007, A&A, 471, 537
Ceverino, D., & Klypin, A. 2009, ApJ, 695, 292
Chen, B. Q., Li, G. X., Yuan, H. B., et al. 2020, MNRAS, 493, 351
Cheng, Y., Tan, J. C., Liu, M., et al. 2018, ApJ, 853, 160
Cheng, Y., Tan, J. C., Caselli, P., et al. 2021, ApJ, 916, 78
Chevance, M., Krumholz, M. R., McLeod, A. F., et al. 2023, in Astronomical Society of the Pacific Conference Series, 534, Protostars and Planets VII, eds. S. Inutsuka, Y. Aikawa, T. Muto, K. Tomida, & M. Tamura, 1

Churchwell, E., Babler, B. L., Meade, M. R., et al. 2009, PASP, 121, 213
Cosentino, G., Jiménez-Serra, I., Henshaw, J. D., et al. 2018, MNRAS, 474, 3760
Cosentino, G., Jiménez-Serra, I., Caselli, P., et al. 2019, ApJ, 881, L42
Cosentino, G., Jiménez-Serra, I., Tan, J. C., et al. 2022, MNRAS, 511, 953
Cosentino, G., Tan, J. C., Jiménez-Serra, I., et al. 2023, A&A, 675, A190
Crapsi, A., Caselli, P., Walmsley, C. M., et al. 2005, ApJ, 619, 379
Dale, J. E. 2015, New A Rev., 68, 1
Dale, J. E., Haworth, T. J., & Bressert, E. 2015, MNRAS, 450, 1199
Dall'Olio, D., Vlemmings, W. H. T., Persson, M. V., et al. 2019, A&A, 626, A36
Emprechtinger, M., Caselli, P., Volgenau, N. H., Stutzki, J., & Wiedner, M. C. 2009, A&A, 493, 89
Fontani, F., Caselli, P., Crapsi, A., et al. 2006, A&A, 460, 709
Fontani, F., Palau, A., Caselli, P., et al. 2011, A&A, 529, L7
Fontani, F., Busquet, G., Palau, A., et al. 2015, A&A, 575, A87
Fontani, F., Barnes, A. T., Caselli, P., et al. 2021, MNRAS, 503, 4320
Friesen, R. K., Kirk, H. M., & Shirley, Y. L. 2013, ApJ, 765, 59
Fuller, G. A., & Myers, P. C. 1992, ApJ, 384, 523
Gerlich, D., Herbst, E., & Roueff, E. 2002, Planet. Space Sci., 50, 1275
Giacani, E. B., Dubner, G. M., Kassim, N. E., et al. 1997, AJ, 113, 1379
Gronenschild, E. H. B. M., Mewe, R., Heise, J., et al. 1978, A&A, 65, L9
Henshaw, J. D., Longmore, S. N., & Kruijssen, J. M. D. 2016, MNRAS, 463, L122
Henshaw, J. D., Jiménez-Serra, I., Longmore, S. N., et al. 2017, MNRAS, 464, L31
Henshaw, J. D., Ginsburg, A., Haworth, T. J., et al. 2019, MNRAS, 485, 2457
Hernandez, A. K., & Tan, J. C. 2015, ApJ, 809, 154
Hoffman, I. M., Goss, W. M., Brogan, C. L., & Claussen, M. J. 2005, ApJ, 627, 803
Inoue, T., Hennebelle, P., Fukui, Y., et al. 2018, PASJ, 70, S53
Inutsuka, S.-i., Inoue, T., Iwasaki, K., & Hosokawa, T. 2015, A&A, 580, A49
Jerabkova, T., Beccari, G., Boffin, H. M. J., et al. 2019, A&A, 627, A57
Jiménez-Serra, I., Martín-Pintado, J., Rodríguez-Franco, A., & Martín, S. 2005, ApJ, 627, L121
Jørgensen, J. K., Hogerheijde, M. R., Blake, G. A., et al. 2004, A&A, 415, 1021
Kainulainen, J., & Tan, J. C. 2013, A&A, 549, A53
Kauffmann, J., Pillai, T., Shetty, R., Myers, P. C., & Goodman, A. A. 2010, ApJ, 716, 433
Kauffmann, J., Pillai, T., & Goldsmith, P. F. 2013, ApJ, 779, 185
Khullar, S., Matzner, C. D., Murray, N., et al. 2024, ApJ, 973, 40
Kong, S., Tan, J. C., Caselli, P., et al. 2016, ApJ, 821, 94
Kong, S., Tan, J. C., Caselli, P., et al. 2017, ApJ, 834, 193
Koo, B.-C., Kim, C.-G., Park, S., & Ostriker, E. C. 2020, ApJ, 905, 35
Krumholz, M. R., & McKee, C. F. 2008, Nature, 451, 1082
Krumholz, M. R., Dekel, A., & McKee, C. F. 2012, ApJ, 745, 69
Kwon, J., Doi, Y., Tamura, M., et al. 2018, ApJ, 859, 4
Larson, R. B. 1981, MNRAS, 194, 809
Lee, Y.-H., Koo, B.-C., & Lee, J.-J. 2020, AJ, 160, 263

Liu, M., Tan, J. C., Cheng, Y., & Kong, S. 2018, ApJ, 862, 105
Liu, X. C., Wu, Y., Zhang, C., et al. 2019, A&A, 622, A32
Martín, S., Martín-Pintado, J., Blanco-Sánchez, C., et al. 2019, A&A, 631, A159
Martin-Pintado, J., Bachiller, R., & Fuente, A. 1992, A&A, 254, 315
Miettinen, O., & Offner, S. S. R. 2013, A&A, 555, A41
Morii, K., Sanhueza, P., Nakamura, F., et al. 2021, ApJ, 923, 147
Oliveira, C. M., Hébrard, G., Howk, J. C., et al. 2003, ApJ, 587, 235
O'Neill, T. J., Cosentino, G., Tan, J. C., Cheng, Y., & Liu, M. 2021, ApJ, 916, 45
Parmentier, G., Kauffmann, J., Pillai, T., & Menten, K. M. 2011, MNRAS, 416, 783
Paron, S., Ortega, M. E., Rubio, M., & Dubner, G. 2009, A&A, 498, 445
Peretto, N., Fuller, G. A., Duarte-Cabral, A., et al. 2013, A&A, 555, A112
Peretto, N., Lenfestey, C., Fuller, G. A., et al. 2016, A&A, 590, A72
Pillai, T., Wyrowski, F., Carey, S. J., & Menten, K. M. 2006, A&A, 450, 569
Pillai, T., Kauffmann, J., Wyrowski, F., et al. 2011, A&A, 530, A118
Pillai, T., Kauffmann, J., Tan, J. C., et al. 2015, ApJ, 799, 74
Pirogov, L., Zinchenko, I., Caselli, P., Johansson, L. E. B., & Myers, P. C. 2003, A&A, 405, 639
Priestley, F. D., Clark, P. C., Glover, S. C. O., et al. 2023, MNRAS, 526, 4952
Punanova, A., Caselli, P., Pon, A., Belloche, A., & André, P. 2016, A&A, 587, A118
Rathborne, J. M., Jackson, J. M., & Simon, R. 2006, ApJ, 641, 389
Reach, W. T., Rho, J., & Jarrett, T. H. 2005, ApJ, 618, 297
Reach, W. T., Rho, J., Tappe, A., et al. 2006, AJ, 131, 1479
Retes-Romero, R., Mayya, Y. D., Luna, A., & Carrasco, L. 2020, ApJ, 897, 53
Rho, J., & Petre, R. 1998, ApJ, 503, L167
Rico-Villas, F., Martín-Pintado, J., González-Alfonso, E., Martín, S., & Rivilla, V. M. 2020, MNRAS, 491, 4573
Rosolowsky, E. W., Pineda, J. E., Kauffmann, J., & Goodman, A. A. 2008, ApJ, 679, 1338
Sánchez-Monge, Á., Palau, A., Fontani, F., et al. 2013, MNRAS, 432, 3288
Sano, H., Inoue, T., Tokuda, K., et al. 2020, ApJ, 904, L24
Sano, H., Yamane, Y., van Loon, J. T., et al. 2023, ApJ, 958, 53
Sashida, T., Oka, T., Tanaka, K., et al. 2013, ApJ, 774, 10
Scheuer, P. A. G. 1963, The Observatory, 83, 56
Schilke, P., Walmsley, C. M., Pineau des Forets, G., & Flower, D. R. 1997, A&A, 321, 293
Shima, K., Tasker, E. J., & Habe, A. 2017, MNRAS, 467, 512
Simon, R., Rathborne, J. M., Shah, R. Y., Jackson, J. M., & Chambers, E. T. 2006, ApJ, 653, 1325
Soam, A., Liu, T., Andersson, B. G., et al. 2019, ApJ, 883, 95
Tan, J. C. 2000, ApJ, 536, 173
Tan, J. C., Beltrán, M. T., Caselli, P., et al. 2014, in Protostars and Planets VI, eds. H. Beuther, R. S. Klessen, C. P. Dullemond, & T. Henning, 149
Tatematsu, K., Umemoto, T., Kandori, R., & Sekimoto, Y. 2004, ApJ, 606, 333
Westerhout, G. 1958, Bull. Astron. Inst. Netherlands, 14, 215
Wootten, A. 1978, Moon Planets, 19, 163
Yoshiike, S., Fukuda, T., Sano, H., et al. 2013, ApJ, 768, 179